Aerodynamic Characterstics of Oval Pattern Grid Fins in Subsonic Regime

Pravalika Puppala
Department of Aerospace Engineeirng
Defence Institue of Advanced Technology
Girinagar. Pune, Maharashtra

Sumit Kumar
Faculty of engineeirng & technology
Shri Khushal Das University
Hanumangarh, Rajasthan
sumitgarg9521@gmail.com

Vipin Yadav
Department of Aerospace Engineeirng
Defence Institue of Advanced Technology
Girinagar. Pune, Maharashtra
vipinyadav.official999@gmai

Dr, Ganapati N. Joshi
Department of Aerospace Engineeirng
Defence Institue of Advanced Technology
Girinagar. Pune, Maharashtra
joshiganapati@gmail.com

doi: https://doi.org/10.37285/bsp.SACAD2025.71

Abstract**:** This study aims to compare the aerodynamic performance of grid fins by examining the impact of grid pattern shape, specifically comparing the traditional square pattern with an oval pattern. Computational Fluid Dynamics (CFD) simulations are utilized across various subsonic Mach numbers (0.3 to 0.8) and angle of attack (0° to 45°) using ANSYS software. To ensure a fair comparison, uniform individual cell surface area and cell numbers are maintained between the two grid patterns. Results show good agreement with the CFD analysis of the square grid pattern, revealing a variation in the coefficient of drag error within 7.5 %. Notably, the oval pattern grid fin demonstrates superior performance at mid-angles of attack (10^0 to 30^0) in subsonic Mach numbers, exhibiting higher lift Coefficient (C_L) and drag coefficient (C_D), as well as an elevated (C_L/C_D) ratio compared to the square pattern grid fin. This study concludes that the oval pattern grid fin offers promising advantages over the traditional square pattern, providing valuable insights for optimizing grid fin design to enhance the aerodynamic efficiency of missiles operating within subsonic flight regimes

Keywords— *Grid fins; Aerodynamic performance; Grid pattern shape; Coefficient of drag; Coefficient of lift.*

I. Introduction

The grid fin is an unconventional control device that consists of the lattice internal structure of a small-length chord. They are also called lattice control surfaces. Extensive research on grid fin is carried out in theoretical, experimental and computational fields. Lattice grid fins have served as crucial control and stability components in a wide array of missiles, bombs, and spacecraft across various nations, including the Soviet Union, the United States, and North Korea. Notably, they have been employed as drag brakes on the Russian SOYUZ TM-22 launch escape spacecraft. More recently, SpaceX's Falcon 9 Reusable Launch Vehicle has adopted these fins for maneuvering during the final stage of re-entry. This versatile technology continues to play a vital role in enhancing the control and maneuverability of aerospace vehicles during critical phases of flight [1].Grid fins have several advantages: Exceptional supersonic control capabilities, compact storage facilitating relatively easy deployment, outstanding high angle of attack performance, minimal center of pressure variations across a broad range of Mach numbers, the capability to customize drag through frame shaping, the ability to adjust lift and drag through fin sweep, high strength-to-weight ratios, and minimal hinge moments reducing actuator demands [2]. Despite their advantages, grid fins also pose several disadvantages as aerodynamic stabilizers or control surfaces. Firstly, they generate higher drag compared to planar fins, particularly in the transonic flight regime. Secondly, their performance diminishes significantly in the transonic regime due to flow choking within individual grid fin cells and the presence of shocks in the flow field. Lastly, their intricate geometry results in high manufacturing costs [3]. Grid fins may consist of an outer frame of various shapes seamlessly linked with a customizable inner grid pattern. Adjusting lift and drag is achievable through thoughtful inner structure design and can be used as a lifting surface, drag brakes and trim tabs [4]. A fine mesh grid fin produces 50% and 150% more normal force than an "X" pattern grid fin at subsonic and supersonic speeds. It produces negligible hinge moments making them effective control devices despite their higher drag characteristics due to the blunt leading edge of the grid fin than the planar fins [5]. The drag increment of the grid fin over the planar fin is about 100% in subsonic and 67% in supersonic regimes [6]. The drag characteristics of a grid fin are notably influenced by the shape of its frame cross-section and the thickness of its web across all speeds simple shaping of these can reduce the drag to considerable levels. Frame cross-section has a greater influence on the normal force at subsonic speeds and web thickness at supersonic speeds while hinge moment has no effect [7]. At low transonic speeds, weak bow shock formation in front of lattice grid fins results in slight flow choking, while at high transonic speeds, strong normal shock formation leads to increased drag. However, at supersonic speeds, the shock is swallowed, resulting in decreased drag [8, 9]. To mitigate drag in the transonic region, a swept-back grid fin with a blunt leading-edge design is proposed, which reduces overall vehicle drag by about 5% and fin drag by 12% compared to conventional grid fins [10,11]. The wind tunnel study on grid fin control effectiveness on missiles and projectiles evaluates them in comparison with planar fins showed increased axial force, decreased normal force, and reduced static stability. Most of the grid fins evaluated are of the square grid pattern with no particular reason so grid fin patterns have become an area of interest. Three grid fin patterns square, triangle and hexagonal with the same cell surface area are evaluated at various Mach numbers. The hexagonal pattern experiences lower normal force at 0.8 Mach as the number of intersection points is more than the square and triangle pattern, choking the flow due to the formation of vortices at intersection points. The normal force depends on the area of each and the total grid cell rather than on the lifting surface. Grid fin pattern has no significant effect on hinge moment and bending moment. So triangular grid fin is more efficient due to its higher structural integrity [23]. The influence grid pattern effects of square, triangular and hexagonal grid fins on aerodynamic characteristics by keeping the dragging area, each cell area and the total grid cell area constant. It is observed that the hexagonal model demonstrates the highest normal force at low Mach. It shows advantages in terms of both aerodynamic stability and drag reduction at supersonic Mach numbers. A hexagonal pattern provides superior aerodynamic performance in various Mach numbers [24]. From the literature survey, it is clear that the grid pattern influences the aerodynamic performance of the grid fin. So, a comparative aerodynamic performance study on an oval grid pattern grid fin which is a novel pattern and a baseline grid fin maintaining equal cell surface area and an equal number of cells at subsonic Mach numbers ranging from 0.3 to 0.8 spanning angle of attack from 0^0 to 45^0 is done. The baseline grid fin is a commonly used square pattern grid fin taken from [23].

II. METHODOLOGY

A Computational Fluid Dynamics (*CFD*) investigation was undertaken to evaluate and compare the aerodynamic characteristics of individual oval and square grid pattern grid fins. This analysis utilized ANSYS Fluent *CFD*, which employs the finite-volume method. The study involved solving the 3D compressible RANS equations, coupled with a turbulence model, and treating the working fluid as air with varying properties. The governing equations for the unsteady compressible turbulent flow in 3D are expressed as follows:

$$\frac{\partial}{\partial x_j}\left(\rho u_j u_i\right) = -\frac{\partial P}{\partial x_i} + \frac{\partial \tau_{ji}}{\partial x_j} \quad \frac{\partial \rho}{\partial t} + \frac{\partial}{\partial x_j}\left(\rho u_j\right) = 0$$

….. (1)

….. (2)

$$\frac{\partial}{x_j}\left(\rho u_j H\right) = \frac{\partial}{\partial x_j}\left[u_i \tau_{ij} + (\mu_{+\sigma} \times \mu_T)\frac{\partial k}{\partial x_j} - q_j\right] \quad \text{….. (3)}$$

Where x_i the position vector, ρ the density, u_i the velocity vector, p the pressure, μ the dynamics viscosity. The total energy is $E=e+u_iu_i/2$ and $H=e+P/\rho+k+u_iu_i/2$, respectively, with $e=p/[(\gamma-1)\rho]$. The term γ is the ratio of specific heats at constant pressure and constant volume.

The computational solver employed the coupled-implicit formulation of Fluent®, enforcing no-slip velocity boundary conditions at the surfaces of the fins. Far-field conditions were meticulously specified for static pressure, temperature, and Mach number. The construction of CAD models was executed meticulously using the ANSYS Design Modeler package. This study carries out *CFD* analysis of both grid fin patterns at a range of subsonic Mach numbers 0.3-0.8 for angle of attack ranging from 0^0 to 45^0.

A. Model Geometry

The baseline grid fin model shown in Fig. 1 was taken from study [25] the geometry details are given in Table I. This grid fin consists of a square grid pattern. The oval pattern grid fin shown in Fig. 2 is modelled by keeping the cell's internal surface area, thickness, chord and no of cells the same as that of the baseline grid fin. The dimensions of the oval pattern grid fin are given in Table 1.

Parameters	Baseline grid fin (in mm)	Oval grid fin (in mm)
Span	8.554	10.84
Height	5.203	7.33
Chord	2.9972	2.9972
Thickness	0.177	0.177
Cell size	1.499	1.61034×2.2802
No of cells	15	15

TABLE I.GEOMETRY PARAMETERS OF BASELINE AND OVAL GRID FIN

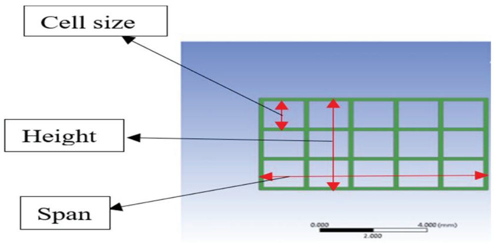

Fig.1. schematic of Baseline grid fin (square cells)

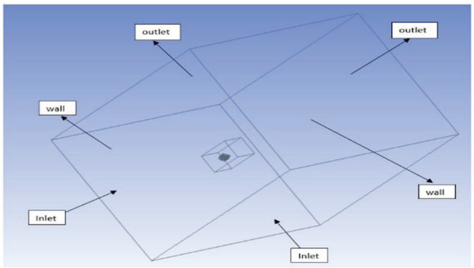

Fig. 1. Schematic of Oval pattern grid fin (Proposed grid fin)

The geometric parameters consist of span (the horizontal length of total grid fin), height (vertical length of total grid fin), chord (fore-to-aft dimension), thickness (cross-sectional dimension) and cell size (the vertical and horizontal lengths inside the cell which are same for square cell).

B. Mesh generation

A computational domain is modelled around both grid fins such that the model is placed at a distance of 5c along the mid-plane from the upstream and 15c from the downstream where c is the length of the chord. A subdomain is created to generate refined mesh around the grid fin. An unstructured hybrid mesh with linear elements is created. Prism layers are generated from the surface of the fin to capture the boundary layer effects on the grid fin. These prism layers are created by considering the initial Y^+ value 1. The first layer distance, denoting the distance from the wall for the initial mesh layer, was finely tuned at 0.001599157mm. A total of 20 layers were incorporated into the mesh with a growth rate of 1.2 to capture the boundary layer effects near the fin surface. Table II shows the mesh details of both models and the Fig. 3 shows the mesh generated on both models.

TABLE II MESH PARAMETERS

Mesh parameter	**Value**
Mesh size on fin	0.1 mm
Mesh Type	Unstructured (hybrid)
Elements	34,00,000
Nodes	11,00,000
Quality (Skewness)	0.26

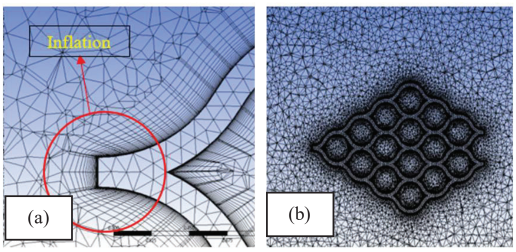

Fig. 2 Fined mesh and inflation layers around oval pattern grid fin.

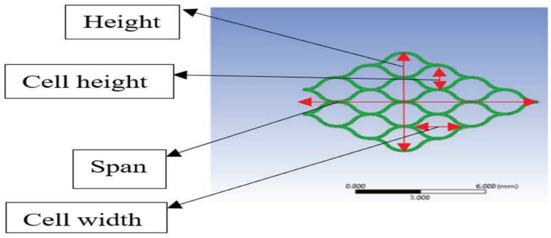

Fig. 3 Boundaries of the computational Domain

C. Flow Conditions

The subsonic flow analysis on both grid fins is carried at Mach numbers ranging from 0.3 to 0.8 at 0.1 intervals. The operating pressure is set to 101325 pa standard atmospheric pressure and the temperature is set to 300 K creating a controlled thermal environment. The investigation is carried out by varying angle of attack values from 0^0 to 45^0 at 5^0 intervals at all Mach numbers. Pressure Far-field boundary conditions are used on the inlet and outlet while no-slip boundary condition is used for the treatment of walls. Fig. 4 shows the boundary locations on both grid fin's computation domains.

D. Solver physics

Pressure-based Reynolds Averaged Navier-Stokes solver of ANSYS FLUENT is used for the current study. Assumptions included the ideal gas equation of state for airflow, while the viscosity-temperature relationship adhered to Sutherland's law. The one-equation Spalart-Allmaras model served as the turbulence model. Discretization of the momentum and energy equations employed a second-order upwind scheme to enhance the accuracy of drag results. The simulations were expedited through the coupled algorithm of the FLUENT solver, ensuring convergence efficiency.

E. Grid Independence Study

A grid-independence study was conducted to confirm that the *CFD* simulation results were independent of mesh resolution. Three mesh configurations-Mesh 1, Mesh 2, and Mesh 3 (as listed in Table III)-were generated while keeping parameters such as global mesh size, first-layer height, and the number of inflation layers (15) constant. Simulations were performed under subsonic conditions for Mach numbers ranging from 0.3 to 0.8, and the resulting C_D were compared with reference data from the literature [25].

TABLE III. MESH CONFIGURATIONS DETAILS

Mesh Configurations	Element size on grid fin (in mm)	Total elements Counts (in million)
Mesh 1	0.8	1.1
Mesh 2	0.1	2.75
Mesh 3	0.06	5.4

As illustrated in Fig. 5, Mesh 1 slightly underestimated C_D values due to insufficient near-wall resolution, resulting in lower prediction of viscous effects. Mesh 3, although highly accurate and closely matching the reference data, required substantially greater computational effort due to its higher cell count. Mesh 2 achieved excellent agreement with the reference results, maintaining deviations within 4% across all Mach numbers while offering significant computational savings compared to Mesh 3. Consequently, Mesh 2 was chosen for subsequent simulations as it offered the best compromise between accuracy and efficiency.

Additionally, a detailed grid-sensitivity analysis was performed by varying the growth ratio (GR) and the number of inflation layers, as shown in Fig. 6(a). GR values of 1.1, 1.2, and 1.5 produced meshes containing approximately 3.8, 2.75, and 2.2 million cells, respectively. Similarly, varying the number of inflation layers (10, 15, and 20) resulted in 2.5, 2.75, and 2.9 million cells, respectively. Among these cases, the configuration with a GR of 1.2 and 15 inflation layers showed the closest match with reference data while maintaining moderate computational cost. Hence, this configuration was adopted for all further simulations to ensure optimal balance between accuracy and computational efficiency.

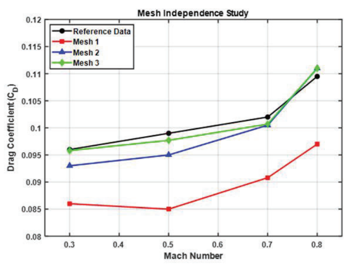

Fig. 5 C_D vs. Mach plot at zero degree angle of attack, at various mesh configuration and compare with reference study data

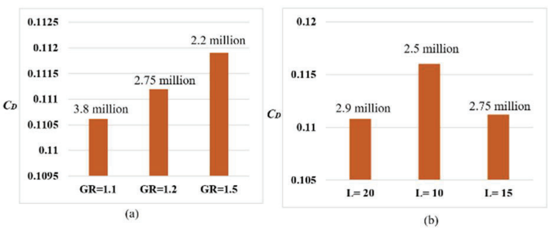

Fig. 6 C_D values at different mesh parameters at Mach 0.8; (a) variation with growth rate at constant number of 15 layers; (b) variation with number of layers at constant growth rate 1.2

F. Validation

The accuracy of the current CFD simulations was validated by comparing the results with reference data reported in the literature [25]. The computed drag coefficient (C_D) at zero angle of attack showed excellent agreement, with a deviation of less than 4%. Fig. 7(a) presents the variation of C_D with Mach number for the reference grid fin configuration. The trend closely matches the reference results, confirming the reliability of the present numerical approach. Both datasets exhibit a steady increase in drag coefficient as the Mach number rises from 0.3 to 0.8, consistent with compressible flow effects where density variations become more pronounced. Over this range, C_D increases from about 0.093 to 0.111- an approximate 19% rise.

At higher angles of attack, as shown in Fig. 7(b), the *CFD* results also align well with the reference data, with a maximum deviation of 7.5% at $\alpha = 10°$, demonstrating the model's capability for accurate high-angle aerodynamic predictions. The drag coefficient values were obtained in the ANSYS Fluent post-processor by integrating viscous and pressure forces over the surfaces of the square and diamond lattice grid fins. Overall, the *CFD* predictions show a strong correlation with previously published numerical data, validating both the accuracy and robustness of the present computational methodology.

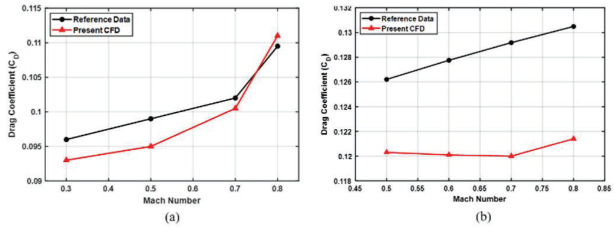

Fig. 7 C_D vs. Mach plot with specific angle of attack, validate and compare C_D value of present *CFD* with reference *CFD* study data; (a) At zero degree angle of attack; (b) at 10° angle of attack

III. RESULTS & DISCUSSION

Aerodynamic Performance Evaluation

The aerodynamic performance of the baseline grid fin and oval pattern grid fin is evaluated by three non-dimensional aerodynamic coefficients- C_L (coefficient of lift), C_D (coefficient of drag) and lift coefficient to drag coefficient ratio (C_L/C_D). These coefficients offer invaluable insights into the abilities of grid fin to generate lift, manage drag and overall efficiency of its aerodynamic profile.

A. Lift Coefficient

The comparative computational fluid dynamics (*CFD*) analysis of the baseline grid fin and oval pattern grid fin across Mach numbers ranging from 0.3 to 0.8, spanning angles of attack from 0° to 45°, shown in Fig.8 reveals consistent trends. Both grid fins exhibit C_L vs. α curves where C_L increases with α until reaching a peak, beyond which it declines, denoting the stall angle, set at 35° for both fins. Notably, the oval pattern grid fin mirrors the trend of the baseline, albeit with consistently higher C_L values. At 0° angle of attack, C_L is negligible for both fins. Moreover, the difference in C_L between the two fins is marginal at lower α, but widens progressively with increasing angles of attack, reaching its peak at higher angles. Furthermore, the average C_L increment between 5° and 45° diminishes with rising Mach numbers from 0.3 to 0.8. The highest increment and average increment in C_L of the oval pattern grid fin over the baseline grid fin is given in Table IV.

TABLE IV. C_L INCREMENT OF OVAL PATTERN GRID FIN OVER BASELINE GRID FIN

Mach Number	Highest increment (%)	Average increment (%) (5^0 to 45^0)
0.3	13.7	12.1877
0.4	13.29	12.21
0.5	12.89	12.22
0.6	12.38	11.98
0.7	12.05	10.64
0.8	13.13	10.38

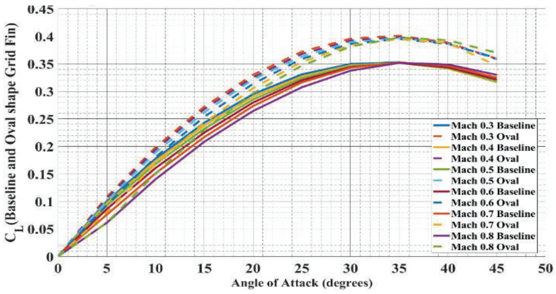

Fig. 8 C_L vs. α of Oval pattern and Baseline grid fin at Mach 0.3 to 0.8

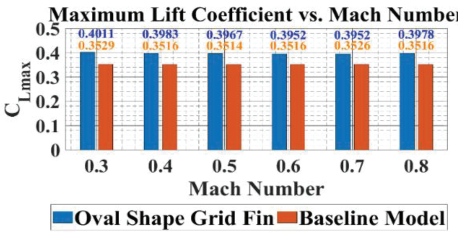

Fig. 9 $(C_L)_{max}$ vs. Mach number at Mach number 0.3 to 0.8

Fig.9 shows the relation between the $(C_L)_{max}$ and Mach number. It is observed that there is no noticeable change in the $(C_L)_{max}$ with Mach number in both the grid fins. We can also observe the increment in $(C_L)_{max}$ of the oval pattern grid over the baseline grid fin which is about 13%.

B. Drag Coefficient (C_D)

The CFD analysis comparing the C_D of the baseline grid fin and oval pattern grid fin across Mach numbers from 0.3 to 0.8, spanning angles of attack from 0° to 45°, shown in Fig.10 reveals consistent patterns. Throughout the range, the C_D of the oval pattern grid fin consistently surpasses that of the baseline. Both fins exhibit a similar trend where drag increases with the angle of attack due to increased wetted area at higher angles. The peak C_D is consistently observed at the highest angle of attack (45°) for both fins across all Mach numbers. Moreover, the disparity in C_D between the two fins widens with increasing angles of attack. Additionally, neither grid fin attains a C_D of zero at 0° angle of attack. Mach number has a negligible effect on Cd till it reaches 0.7 in the mid-range angle of attack 20^o to 40^o. The highest increment and average increment in C_D of the oval pattern grid fin over the baseline grid fin is given in Table V. The peak C_D is consistently observed at the highest α = 45° for both fins across all Mach numbers. Moreover, the disparity in C_D between the two fins widens with increasing angles of attack. Additionally, neither grid fin attains a C_D of zero at 0° angle of attack. Mach number has a negligible effect on Cd till it reaches 0.7 in the mid-range angle of attack 20^o to 40^o. The highest increment and average increment in C_D of the oval pattern grid fin over the baseline grid fin is given in Table V.

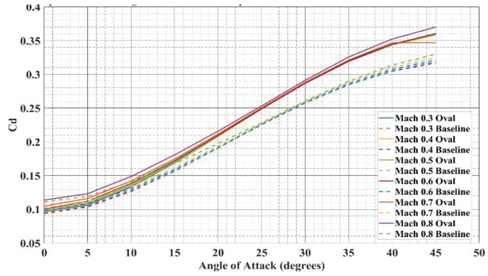

Fig. 10 C_D vs. α plots of Oval pattern and Baseline grid fin at Mach number 0.3 to 0.8

TABLE V. AVERAGE C_D INCREMENT

Mach number	Highest Increment (%)	Average increment (%) (0^0 to 45^0)
0.3	13.39	8.86
0.4	12.94	8.79
0.5	12.52	8.54
0.6	12.17	8.72
0.7	11.74	8.075
0.8	12.39	8.773

C. Lift to drag coefficient ratio (C_L/C_D)

The comprehensive CFD analysis of the baseline grid fin and oval pattern grid fin for their aerodynamic efficiency, represented by the lift coefficient to drag coefficient ratio (C_L/C_D), across Mach numbers, ranging from 0.3 to 0.8 and angles of attack from 0° to 45° shown in Fig.11, reveals consistent behaviors. The (C_L/C_D) curve demonstrates a uniform trend for both fins, where it initially rises with increasing angle of attack, reaching a peak before declining. Across all simulated Mach numbers, the aerodynamic efficiency of the oval pattern grid fin consistently surpasses that of the baseline. At 0° angle of attack, both fins exhibit negligible lift, resulting in a (C_L/C_D) value of zero. Conversely, at the maximum angle of attack (45°), both fins achieve identical C_L and C_D values, resulting in a (C_L/C_D) ratio of 1. Furthermore, the increment in (C_L/C_D) ratio for the oval pattern grid fin is comparatively smaller at lower and higher angles of attack. The increment is more prominent in mid-angles of attack. The highest increment and average increment in *(C_L/C_D)* of the oval pattern grid fin over the baseline grid fin is given in Table VI.

Mach number	Highest increment (%)	Average increment (%) (5^0 to 40^0)
0.3	5.84	2.775
0.4	5.9	2.88
0.5	5.95	2.86
0.6	5.82	2.62
0.7	4.72	2.05
0.8	2.52	1.49 (10^0 to 40^0)

TABLE VI. AVERAGE % INCREMNET IN (C_L/C_D)

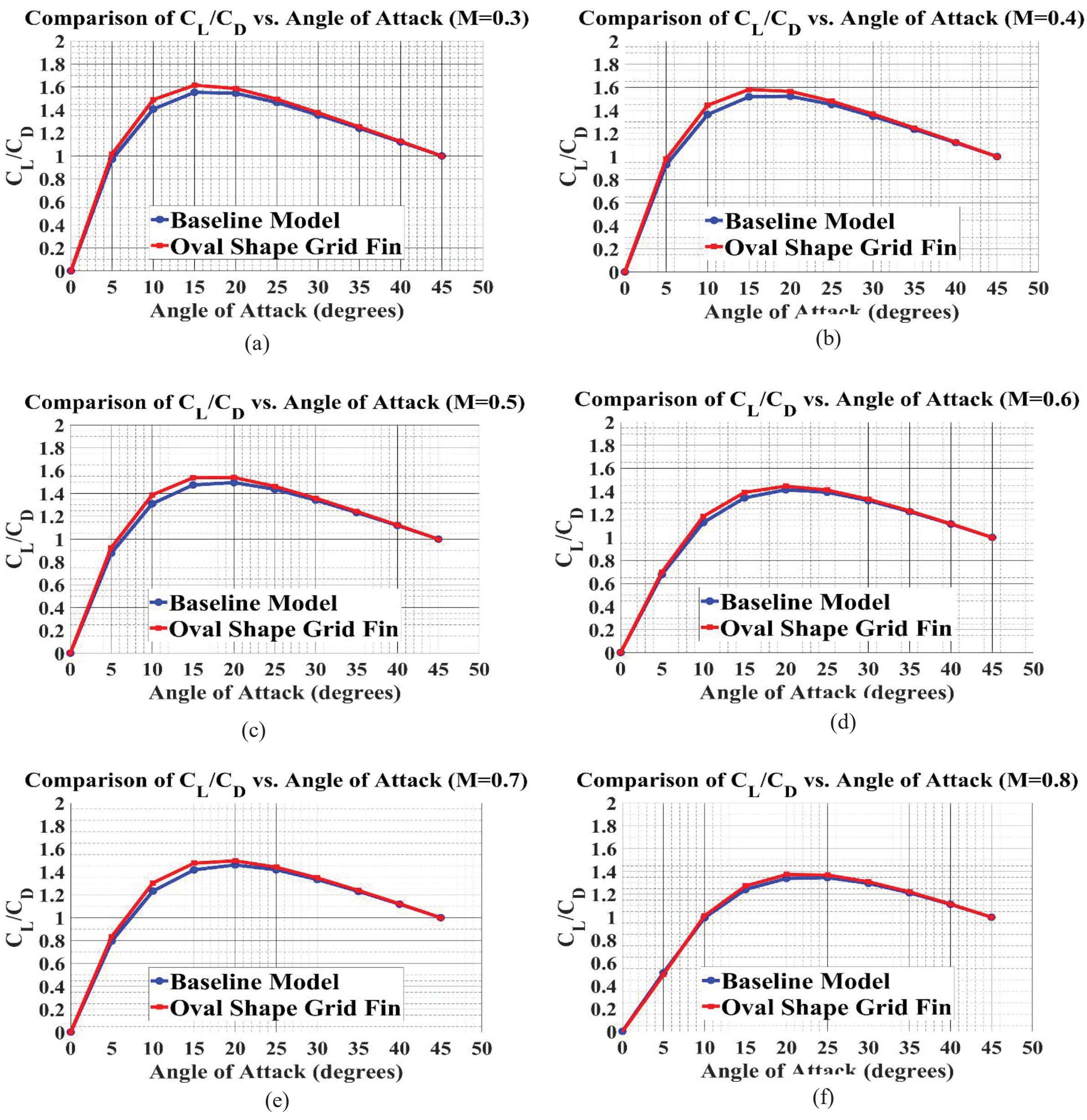

Fig.11 (*C_L/C_D*) vs. *α* curve for comparison wise trend of oval and square grid fin at; (a) M=0.3; (b) M=0.4; (c) M=0.5; (d) M=0.6; (e) M=0.7; (f) M=0.8

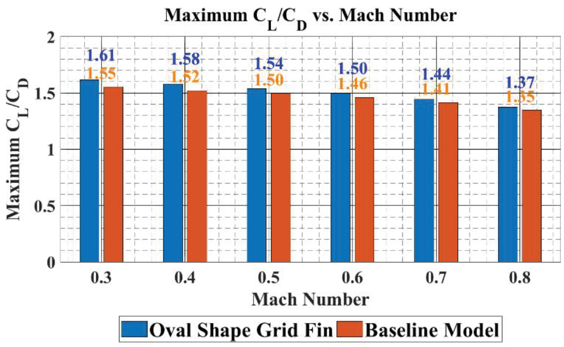

Fig.12 Maximum (C_L/C_D) Value variation over both grid fin models at Mach 0.3 to 0.8

The relation between $(C_L/C_D)_{max}$ vs. Mach number is shown in Fig. 12. The maximum aerodynamic efficiency reduces with an increase in the Mach number. Even the $(C_L)_{max}$ is independent of the Mach number $(C_L/C_D)_{max}$ decreases with the Mach number due to the increment of Cd as the Mach number reaches transonic speeds. The $(C_L/C_D)_{max}$ of the oval pattern is higher than that of the baseline grid fin. The increment of $(C_L/C_D)_{max}$ decreases as the Mach number increases ranging from 3.87% to 1.48%.

D. Flow visualization

From the Mach contours of both the oval-pattern and baseline grid fins shown in Fig.13, it can be observed that, when subjected to a free-stream Mach number of 0.8 at α of 35°, the local Mach number within the upper half of the grid fin cells increases up to approximately 0.4. This indicates localized flow acceleration due to the geometry of the grid fin. As shown in Fig.13, when the flow angle is maintained at $\alpha = 35°$, the Mach number reaches sonic conditions within several individual cells of both fin configurations. This effect is particularly pronounced in the upper cells, where choking occurs-more than half of the upper cell regions become choked, significantly reducing the available flow area. When compared with the baseline grid fin, the oval-pattern grid fin exhibits fewer choked cells, but the choked surface area per cell is larger, leading to increased flow resistance and, consequently, higher drag. The pressure distribution illustrated in Fig.14 further clarifies this behavior. The pressure on the lower surfaces of the horizontal members is notably higher than on the upper surfaces, generating lift on the grid fin. Additionally, the leading edge experiences higher pressure, while the trailing edge exhibits a lower pressure region, resulting in suction that enhances aerodynamic performance. The oval-pattern grid fin contains a greater number of horizontal members than the baseline design, which increases the effective lifting surface area and thus results in a higher lift coefficient (C_L).

This pressure difference is most significant at α = 35°, explaining why the maximum lift coefficient $(C_L)_{max}$ occurs at this angle across all Mach numbers. Moreover, since the pressure differential pattern remains relatively consistent at different Mach numbers, the $(C_L)_{max}$ values are nearly identical for all tested flow conditions.

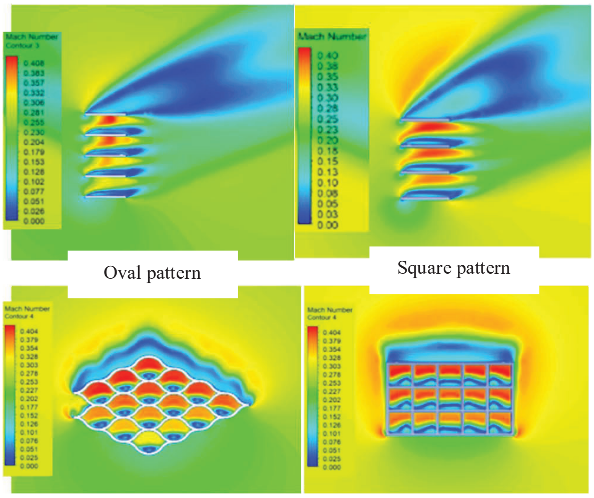

Fig. 13 Mach contour on Oval pattern and square grid fin at 35^0 and M=0.8

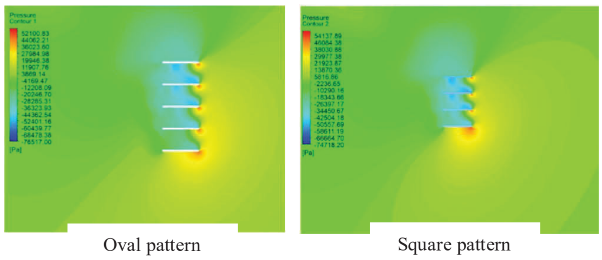

Fig. 14 Pressure contour on Oval patter Square grid fin at 35^0 and M=0.8

IV. CONCLUSION

The *CFD* analysis of baseline and oval pattern grid fin at Mach number ranging from 0.3 to 0.8 spanning 0^0 to 45^0 angle of attack is done using ANSYS FLUENT 2021. The aerodynamic parameters of both grid fins are analyzed and compared. This analysis concludes that:

1. The C_L of both grid fins follow the same trend, C_L increases with α after reaching its maximum at a stall angle of 35^0 it decreases with α. A negligible C_L is produced at 0^0 α for all Mach numbers. The oval pattern grid fin produces a high C_L compared to the baseline grid fin as the number of horizontal members is greater in the oval pattern grid fin.
2. The C_D of both grid fins follows the same trend, C_D increases with an increase in α. The C_D of the oval pattern grid fin is higher than the baseline grid fin. The maximum increment occurs at low Mach numbers. The C_D increases with the Mach number as chocking of individual cells occurs at transonic speeds.
3. The (C_L/C_D) of the oval pattern grid fin is higher than the baseline grid fin at mid angles. It is also observed that at low Mach numbers, the increment

is large. The (C_L/C_D) produced at 45^0 α is always 1 for both grid fins at all Mach numbers. $(C_L/C_D)_{max}$ decreased with increasing in Mach number as C_D increases.

4. The oval pattern grid fin shows superiority in terms of C_L and (C_L/C_D), but C_D is higher than the baseline which can reduced by modifying the blunt leading edge to sharp. Oval pattern grid fin aerodynamic efficiency is higher at the mid angles of attack10^0 to 35^0.

The oval pattern grid fin can be modified by changing the rectangular cross-section of the horizontal members to a wedge shape by sharpening the leading edge to reduce the drag. The *CFD* analysis of the oval pattern grid fin should be done at supersonic speeds to analyze its performance at those speeds. The comparative study of oval pattern grid fin should be done with hexagonal grid fin which is the nearer geometrical shape. Analysis can be carried out by changing the thickness of members and gap height to optimize the design. Analysis of sweep backwards or sweep forward grid fins along the vertical axis of grid fin with oval pattern can be done.

REFERENCES

[1] M. Tripathi, A. Misra, and M. M. Sucheendran, "Effect of rectangular and airfoil planar member cross-section on cascade fin aerodynamics," in Proc. AIAA Atmospheric Flight Mechanics Conf., 2018, doi: 10.2514/6.2018-1761.

[2] W. D. Washington and M. S. Miller, "Experimental investigations of grid fin aerodynamics: A synopsis of nine wind tunnel and three flight tests," in Proc. AGARD Appl. Vehicle Technol. Panel Symp. Missile Aerodynamics, Paper 10, May 1998.

[3] T. W. Ledlow, J. E. Burkhalter, and R. J. Hartfield, "Integration of grid fins for the optimal design of missile systems," in Proc. AIAA Atmospheric Flight Mechanics Conf., 2015, doi: 10.2514/6.2015-1017.

[4] R. A. Brooks and J. E. Burkhalter, "Experimental and analytical analysis of grid fin configurations," J. Aircraft, vol. 26, no. 9, pp. 885–887, 1989, doi: 10.2514/3.45856.

[5] W. Washington and M. Miller, "Grid fins – A new concept for missile stability and control," in Proc. 31st AIAA Aerospace Sciences Meeting, 1993, AIAA Paper 1993-35, doi: 10.2514/6.1993-35.

[6] G. Abate, R. Duckerschein, and W. Hathaway, "Subsonic/transonic free-flight tests of a generic missile with grid fins," in Proc. 38th AIAA Aerospace Sciences Meeting and Exhibit, 2000, doi: 10.2514/6.2000-937.

[7] M. Miller and W. Washington, "An experimental investigation of grid fin drag reduction techniques," in Proc. 12th AIAA Applied Aerodynamics Conf., 1994, AIAA Paper 1994-1914, doi: 10.2514/6.1994-1914.

[8] M. Hughson, E. Blades, and G. Abate, "Transonic aerodynamic analysis of lattice grid tail fin missiles," in Proc. 24th AIAA Applied Aerodynamics Conf., 2006, doi: 10.2514/6.2006-3651.

[9] M. Hughson, E. Blades, E. Luke, and G. Abate, "Analysis of lattice grid tailfin missiles in high-speed flow," in Proc. 25th AIAA Applied Aerodynamics Conf., 2007, doi: 10.2514/6.2007-3932.

[10] Y. Zeng, J. Cai, M. Debiasi, and T. L. Chng, "Numerical study on drag reduction for grid-fin configurations," in Proc. 47th AIAA Aerospace Sciences Meeting including The New Horizons Forum and Aerospace Exposition, Jan. 2009, doi: 10.2514/6.2009-1105.

[11] J. Cai, "Numerical study on choked flow over grid-fin configurations," J. Spacecraft Rockets, vol. 46, no. 5, pp. 949–956, 2009, doi: 10.2514/1.41442.

[12] M. Debiasi, Z. Yan, and T. L. Chng, "Swept-back grid fins for transonic drag reduction," in Proc. 28th AIAA Applied Aerodynamics Conf., 2010, doi: 10.2514/6.2010-4244.

[13] M. Debiasi, "Measurements of the forces and moments generated by swept-back grid fins," in Proc. 30th AIAA Applied Aerodynamics Conf., 2012, doi: 10.2514/6.2012-2909.

[14] M. Debiasi and Y. Zeng, "Forces and moments generated by swept-back grid fins with sharp leading edges," J. Aircraft, vol. 53, no. 6, pp. 1964–1968, 2016, doi: 10.2514/1.C033504.

[15] Y. Zeng, "Drag reduction for sweptback grid fin with blunt and sharp leading edges," J. Aircraft, vol. 49, no. 5, pp. 1526–1531, 2012, doi: 10.2514/1.C031653.

[16] M. Debiasi, "Forces and moments generated by swept-forward grid fins and planar fins," J. Aircraft, vol. 57, no. 1, pp. 167–172, 2020, doi: 10.2514/1.C035626.

[17] D. Wang and Y. Yu, "Numerical study on drag reduction for swept-back, swept-front, delta grid fin with blunt and sharp leading edges," in Proc. AIAA Modeling and Simulation Technologies Conf., 2014, doi: 10.2514/6.2014-0638.

[18] E. Fournier, "Wind tunnel investigation of grid fin and conventional planar control surfaces," in Proc. 39th AIAA Aerospace Sciences Meeting and Exhibit, 2001, doi: 10.2514/6.2001-256.

[19] C. Bernier and A. Dupuis, "Wind tunnel tests of a grid finned projectile configuration," in Proc. 39th AIAA Aerospace Sciences Meeting and Exhibit, 2001, doi: 10.2514/6.2001-105.

[20] J. DeSpirito, M. Vaughn, and W. Washington, "Subsonic flow CFD investigation of canard-controlled

missile with planar and grid fins," in Proc. 41st AIAA Aerospace Sciences Meeting and Exhibit, 2003, doi: 10.2514/6.2003-27.

[21] D. Pruzan, M. Mendenhall, W. Rose, and D. Schuster, "Grid fin stabilization of the Orion launch abort vehicle," in Proc. 29th AIAA Applied Aerodynamics Conf., 2011, doi: 10.2514/6.2011-3018.

[22] J. Kless and M. Aftosmis, "Analysis of grid fins for launch abort vehicle using a Cartesian Euler solver," in Proc. 29th AIAA Applied Aerodynamics Conf., 2011, doi: 10.2514/6.2011-3666.

[23] F. Hiroshima and K. Tatsumi, "Grid pattern effects –on aerodynamic characteristics of grid fins," in Proc. 4th Int. Congr. Aeronaut. Sci., 2004, pp. 1–8.

[24] V.-S. Dinh, C.-T. Dinh, and V.-S. Pham, "Numerical study on aerodynamic characteristics of the grid fins with different grid patterns," Phys. Fluids, vol. 35, no. 12, p. 123117, Dec. 2023.

[25] A. Despeyroux, F. Chopard, L. Petit, and P. Duthoit, "Numerical analysis of static and dynamic performances of grid fin controlled missiles," J. Spacecraft Rockets, vol. 52, no. 4, pp. 1236–1252, 2015, doi: 10.2514/1.A33189.